A terrestrial planet candidate in a temperate orbit around Proxima Centauri

Guillem Anglada-Escudé[1*], Pedro J. Amado[2], John Barnes[3], Zaira M. Berdiñas[2], R. Paul Butler[4], Gavin A. L. Coleman[1], Ignacio de la Cueva[5], Stefan Dreizler[6], Michael Endl[7], Benjamin Giesers[6], Sandra V. Jeffers[6], James S. Jenkins[8], Hugh R. A. Jones[9], Marcin Kiraga[10], Martin Kürster[11], María J. López-González[2], Christopher J. Marvin[6], Nicolás Morales[2], Julien Morin[12], Richard P. Nelson[1], José L. Ortiz[2], Aviv Ofir[13], Sijme-Jan Paardekooper[1], Ansgar Reiners[6], Eloy Rodríguez[2], Cristina Rodríguez-López[2], Luis F. Sarmiento[6], John P. Strachan[1], Yiannis Tsapras[14], Mikko Tuomi[9], Mathias Zechmeister[6].

July 13, 2016

[1]School of Physics and Astronomy, Queen Mary University of London, 327 Mile End Road, London E1 4NS, UK

[2]Instituto de Astrofsica de Andaluca - CSIC, Glorieta de la Astronoma S/N, E-18008 Granada, Spain

[3]Department of Physical Sciences, Open University, Walton Hall, Milton Keynes MK7 6AA, UK

[4]Carnegie Institution of Washington, Department of Terrestrial Magnetism 5241 Broad Branch Rd. NW, Washington, DC 20015, USA

[5]Astroimagen, Ibiza, Spain

[6]Institut für Astrophysik, Georg-August-Universität Göttingen Friedrich-Hund-Platz 1, 37077 Göttingen, Germany

[7]The University of Texas at Austin and Department of Astronomy and McDonald Observatory 2515 Speedway, C1400, Austin, TX 78712, USA

[8]Departamento de Astronoma, Universidad de Chile Camino El Observatorio 1515, Las Condes, Santiago, Chile

[9]Centre for Astrophysics Research, Science & Technology Research Institute, University of Hertfordshire, Hatfield AL10 9AB, UK

[10]Warsaw University Observatory, Aleje Ujazdowskie 4, Warszawa, Poland

[11]Max-Planck-Institut für Astronomie Königstuhl 17, 69117 Heidelberg, Germany

[12]Laboratoire Univers et Particules de Montpellier, Universit de Montpellier, Pl. Eugène Bataillon - CC 72, 34095 Montpellier Cédex 05, France

[13]Department of Earth and Planetary Sciences, Weizmann Institute of Science, 234 Herzl Street,

Rehovot 76100, Israel
[14]Astronomisches Rechen-Institut, Mönchhofstrasse 12-14 69120 Heidelberg Germany

*Corresponding author E-mail: g.anglada@qmul.ac.uk
Authors listed in alphabetical order after corresponding author.

At a distance of 1.295 parsecs,[1] the red-dwarf Proxima Centauri (α Centauri C, GL 551, HIP 70890, or simply Proxima) is the Sun's closest stellar neighbour and one of the best studied low-mass stars. It has an effective temperature of only $\sim$ 3050 K, a luminosity of $\sim$0.1 per cent solar, a measured radius of 0.14 $R_\odot$[2] and a mass of about 12 per cent the mass of the Sun. Although Proxima is considered a moderately active star, its rotation period is $\sim$ 83 days,[3] and its quiescent activity levels and X-ray luminosity[4] are comparable to the Sun's. New observations reveal the presence of a small planet orbiting Proxima with a minimum mass of 1.3 Earth masses and an orbital period of $\sim$11.2 days. Its orbital semi-major axis is ~ 0.05 AU, with an equilibrium temperature in the range where water could be liquid on its surface.[5]

The results presented here consist of the analysis of previously obtained Doppler measurements (pre-2016 data), and the confirmation of a signal in a specifically designed follow-up campaign in 2016. The Doppler data comes from two precision radial velocity instruments, both at the European Southern Observatory (ESO): the High Accuracy Radial velocity Planet Searcher (HARPS) and the Ultraviolet and Visual Echelle Spectrograph (UVES). HARPS is a high-resolution stabilized echelle spectrometer installed at the ESO 3.6m telescope (La Silla observatory, Chile), and is calibrated in wavelength using hollow cathode lamps (Th Ar). HARPS has demonstrated radial velocity measurements at $\sim$1 ms^{-1}precision over time-scales of years,[6] including on low-mass stars.[7] All HARPS spectra were extracted and calibrated with the standard ESO Data Reduction Software, and radial velocities were measured using a least-squares template matching technique.[7] HARPS data is separated into two datasets. The first set includes all data obtained before 2016 by several programmes (HARPS pre-2016). The second HARPS set comes from the more recent *Pale Red Dot* campaign (PRD hereafter), which was designed to eliminate period ambiguities using new HARPS observations and quasi-simultaneous photometry. The HARPS PRD observations consisted of obtaining one spectrum almost every night between Jan 19th and March 31st 2016. The UVES observations used the Iodine cell technique[8] and were obtained in the framework of the UVES survey for terrestrial planets around M-dwarfs between 2000 and 2008. The spectra were extracted using the standard procedures of the UVES survey,[9] and new radial velocities were re-obtained using up-to-date Iodine reduction codes.[10] Since systematic calibration errors produce correlations among observations within each night,[11] we consolidated Doppler measurements through nightly averages to present a simpler and more conservative signal search. This led to 72 UVES, 90 HARPS pre-2016 and 54 HARPS PRD epochs. The PRD photometric observations were obtained using the Astrograph for the South Hemisphere II telescope (ASH2 hereafter,[12] SII and H_α narrowband filters) and the Las Cumbres Observatory Global Telescope network (LCOGT.net,[13] Johnson B and V bands), over the same time interval and similar sampling as the HARPS PRD observations. Further details about

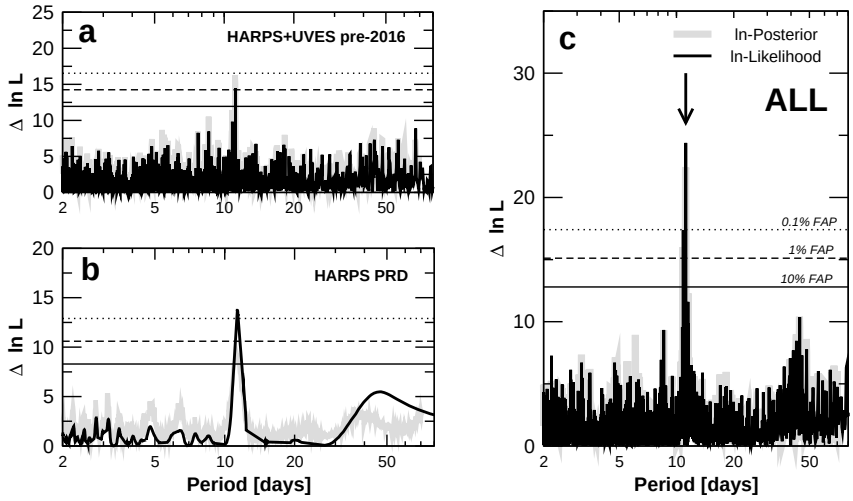

Figure 1: **Detection of a Doppler signal at 11.2 days**. Detection periodograms of the 11.2 day signal in the HARPS+UVES pre-2016 data (panel a), and using the HARPS Pale Red Dot campaign only (panel b). Panel c contains the periodogram obtained after combining all datasets. Black lines correspond to the $\Delta \ln L$ statistic, while the gray thick represent the logarithm of the Bayesian posterior density (see text, arbitrary vertical offset applied to for visual comparison of the two statistics). The horizontal solid, dashed and dotted lines represent a 10, 1, and 0.1 per cent false alarm probability thresholds of the frequentist analysis, respectively.

each campaign and the photometry are detailed in the methods section. All time-series used in this work in the online version of the paper as Source data.

The search and significance assessment of signals were performed using frequentist[14] and Bayesian[15] methods. Periodograms in Figure 1 represent the improvement of some reference statistic as a function of trial period, with the peaks representing the most probable new signals. The improvement in the logarithm of the likelihood function $\Delta \ln L$ is the reference statistic used in the frequentist framework, and its value is then used to assess the false-alarm probability (or FAP) of the detection.[14] A FAP below 1% is considered suggestive of periodic variability, and anything below 0.1% is considered to be a significant detection. In the Bayesian framework, signals are first searched using a specialized sampling method[16] that enables exploration of multiple local maxima of the posterior density (the result of this process are the red lines in Figure 1), and significances are then assessed by obtaining the ratios of *evidences* of models. If the evidence ratio between two models exceeds some threshold (e.g. $B_1/B_0 > 10^3$), then the model in the numerator (with one planet) is favoured against the model in the denominator (no planet).

A well isolated peak at $\sim$11.2 days was recovered when analyzing all the night averages in the pre-2016 datasets (Figure 1, panel a). Despite the significance of the signal, the analysis of pre-2016 subsets produced slightly different periods depending on the noise assumptions and which subsets were considered. Confirmation or refutation of this signal at 11.2 days was the main driver for proposing the HARPS PRD campaign. The analysis of the HARPS PRD data revealed a single significant signal at the same $\sim 11.3 \pm 0.1$ day period (Figure 1, panel b), but period coincidence

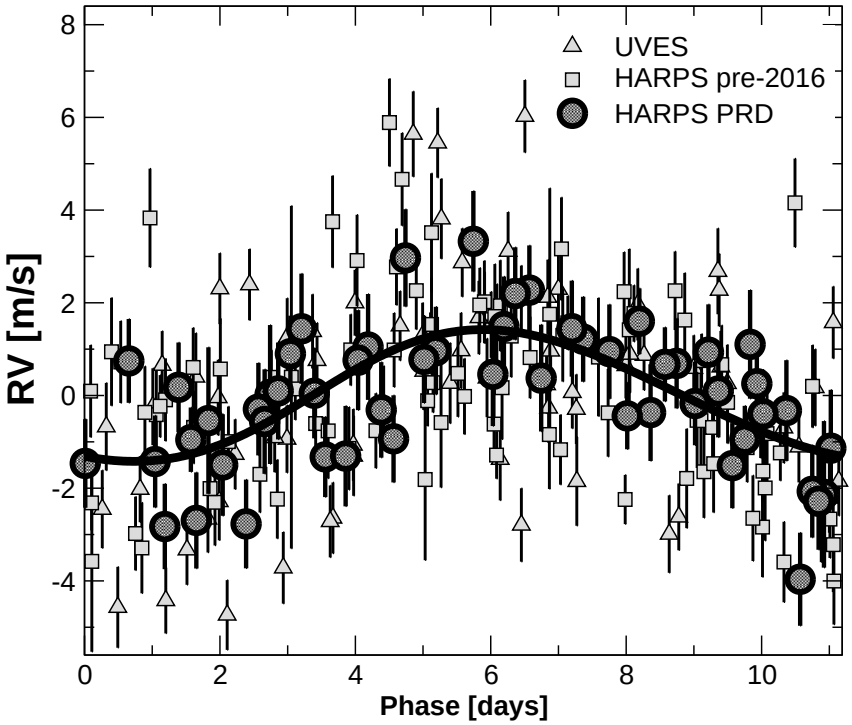

Figure 2: **All datasets folded to the 11.2 days signal**. Radial velocity measurements phase folded at the 11.2 day period of the planet candidate for 16 years of observations. Although its nature is unclear, a second signal at P$\sim$ 200 days was fitted and subtracted from the data to produce this plot and improve visualization. Circles correspond to HARPS PRD, triangles are HARPS pre-2016 and squares are UVES. The black line represents the best Keplerian fit to this phase folded representation of the data. Error bars correspond to formal 1-σ uncertainties.

alone does not prove consistency with the pre-2016 data. Final confirmation is achieved when all the sets were combined (Figure 1, panel c). In this case statistical significance of the signal at 11.2 days increases dramatically (false-alarm probability $< 10^{-7}$, Bayesian evidence ratio $B_{1,0} > 10^6$). This implies that not only the period, but also the amplitude and phase are consistent during the 16 years of accumulated observations (see Figure 2). All analyses performed with and without correlated-noise models produced consistent results. A second signal in the range of 60 to 500 days was also detected, but its nature is still unclear due to stellar activity and inadequate sampling.

Stellar variability can cause spurious Doppler signals that mimic planetary candidates, especially when combined with uneven sampling.[9,17] To address this, the time-series of the photometry and spectroscopic activity indices were also searched for signals. After removing occasional flares, all four photometric time-series show the same clear modulation over $P \sim 80$ nights (panels b, c, d and e in Figure 3), which is consistent with the previously reported photometric period of $\sim$83 d.[3] Spectroscopic activity indices were measured on all HARPS spectra, and their time-series were investigated as well. The width of the spectral lines (measured as the variance of the mean line, or m_2) follows a time-dependence almost identical to the light curves, a behaviour that has already

been reported for other M-dwarf stars.[18] The time-series of indices based on chromospheric emission lines (e.g. H_α) do not show evidence of periodic variability, even after removing data points likely affected by flares. We also investigated possible correlations of the Doppler measurements with activity indices by including linear correlation terms in the Bayesian model of the Doppler data. While some indices do show hints of correlation in some campaigns, including them in the model produces lower probabilities due to overparameterization. Flares have very little effect on our Doppler velocities, as has already been suggested by previous observations of Proxima.[19] More details are provided in the methods section and as Extended Data Figures. Since the analysis of the activity data failed to identify any stellar activity feature likely to generate a spurious Doppler signal at 11.2 days, we conclude that the variability in the data is best explained by the presence of a planet (Proxima b, hereafter) orbiting the star. All available photometric light curves were searched for evidence of transits, but no obvious transit-like features were detectable in our light curves. We used Optimal Box-Least-Squares codes[20] to search for candidate signals in data from the All Sky Automatic Survey.[3] No significant transit signal was found down to a depth of about 5% either. The preferred orbital solution and the putative properties of the planet and transits are given in Table 1.

The Doppler semi-amplitude of Proxima b (~ 1.4 ms^{-1}) is not particularly small compared to other reported planet candidates.[6] The uneven and sparse sampling combined with longer-term variability of the star seem to be the reasons why the signal could not be unambiguously confirmed with pre-2016 rather than the amount of data accumulated. The corresponding minimum planet mass is ~ 1.3 $M_\oplus$. With a semi-major axis of $\sim$0.05 AU, it lies squarely in the center of the classical habitable zone for Proxima.[5] As mentioned earlier, the presence of another super-Earth mass planet cannot yet be ruled out at longer orbital periods and Doppler semi-amplitudes <3 ms^{-1}. By numerical integration of some putative orbits, we verified that the presence of such an additional planet would not compromise the orbital stability of Proxima b.

Habitability of planets like Proxima b -in the sense of sustaining an atmosphere and liquid water on its surface- is a matter of intense debate. The most common arguments against habitability are tidal locking, strong stellar magnetic field, strong flares, and high UV & X-ray fluxes; but none of these have been proven definitive. Tidal locking does not preclude a stable atmosphere via global atmospheric circulation and heat redistribution.[22] The average global magnetic flux density of Proxima is 600$\pm$150 Gauss,[23] which is quite large compared to the Sun's value of 1 G. However, several studies have shown that planetary magnetic fields in tidally locked planets can be strong enough to prevent atmospheric erosion by stellar magnetic fields[24] and flares,.[25] Because of its close-in orbit, Proxima b suffers X-ray fluxes $\sim$400 times that of Earth's, but studies of similar systems indicate that atmospheric losses can be relatively small.[26] Further characterization of such planets can also inform us about the origin and evolution of terrestrial planets. For example, forming Proxima b from in-situ disk material is implausible because disk models for small stars would contain less than 1 $M_{\rm Earth}$ of solids within the central AU. Instead, either 1) the planet migrated in via type I migration,[27] 2) planetary embryos migrated in and coalesced at the current planet's orbit, or 3) pebbles/small planetesimals migrated via aerodynamic drag[28] and later coagulated into a larger body. While migrated planets and embryos originating beyond the ice-line would be volatile rich, pebble migration would

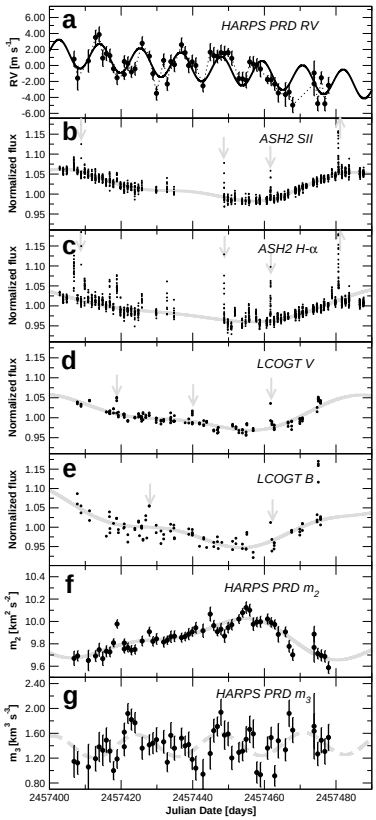

Figure 3: **Time-series obtained during the Pale Red Dot campaign**. HARPS-PRD radial velocity measurements (panel a), quasi-simultaneous photometry from ASH2 (panels b and c) and LCOGT (panels d and e) and central moments of the mean line profiles (panels f and g). The solid lines show the best fits. A dashed line indicates a signal that is not sufficiently significant. Excluded measurements likely affected activity events (e.g. flares) are marked with grey arrows. The photometric time-series and m_2 all show evidence of the same $\sim$80 day modulation. Error bars correspond to formal 1-σ uncertainties.

produce much drier worlds. In this sense, a warm terrestrial planet around Proxima offers unique follow-up opportunities to attempt further characterization via transits -on going searches-, via direct imaging and high-resolution spectroscopy in the next decades,[29] and –maybe– robotic exploration in the coming centuries.[30]

References

[1] van Leeuwen, F. Validation of the new Hipparcos reduction. *Astron. Astrophys.* **474**, 653–664 (2007).

[2] Boyajian, T. S. *et al.* Stellar Diameters and Temperatures. II. Main-sequence K- and M-stars. *Astrophys. J.* **757**, 112 (2012).

[3] Kiraga, M. & Stepien, K. Age-Rotation-Activity Relations for M Dwarf Stars. *AcA* **57**, 149–172 (2007).

[4] Güdel, M., Audard, M., Reale, F., Skinner, S. L. & Linsky, J. L. Flares from small to large: X-ray spectroscopy of Proxima Centauri with XMM-Newton. *Astron. Astrophys.* **416**, 713–732 (2004).

[5] Kopparapu, R. K. *et al.* Habitable Zones around Main-sequence Stars: New Estimates. *Astrophys. J.* **765**, 131 (2013).

[6] Pepe, F. *et al.* The HARPS search for Earth-like planets in the habitable zone. I. Very low-mass planets around HD 20794, HD 85512, and HD 192310. *Astron. Astrophys.* **534**, A58+ (2011).

[7] Anglada-Escudé, G. & Butler, R. P. The HARPS-TERRA Project. I. Description of the Algorithms, Performance, and New Measurements on a Few Remarkable Stars Observed by HARPS. *Astrophys. J. Suppl.* **200**, 15 (2012).

[8] Butler, R. P. *et al.* Attaining Doppler Precision of 3 M s-1. *Proc. Astron. Soc. Pacific* **108**, 500–+ (1996).

[9] Kürster, M. *et al.* The low-level radial velocity variability in Barnard's star (= GJ 699). Secular acceleration, indications for convective redshift, and planet mass limits. *Astron. Astrophys.* **403**, 1077–1087 (2003).

[10] Arriagada, P. *et al.* Two Planetary Companions around the K7 Dwarf GJ 221: A Hot Super-Earth and a Candidate in the Sub-Saturn Desert Range. *Astrophys. J.* **771**, 42 (2013).

[11] Berdiñas, Z. M., Amado, P. J., Anglada-Escudé, G., Rodríguez-López, C. & Barnes, J. High-cadence spectroscopy of M-dwarfs. I. Analysis of systematic effects in HARPS-N line profile measurements on the bright binary GJ 725A+B. *ArXiv e-prints* (2016).

[12] Sicardy, B. *et al.* A Pluto-like radius and a high albedo for the dwarf planet Eris from an occultation. *Nature* **478**, 493–496 (2011).

[13] Brown, T. M. *et al.* Las Cumbres Observatory Global Telescope Network. *Proc. Astron. Soc. Pacific* **125**, 1031–1055 (2013).

[14] Baluev, R. V. The impact of red noise in radial velocity planet searches: only three planets orbiting GJ 581? *Mon. Not. R. Astron. Soc* **429**, 2052–2068 (2013).

[15] Tuomi, M., Jones, H. R. A., Barnes, J. R., Anglada-Escudé, G. & Jenkins, J. S. Bayesian search for low-mass planets around nearby M dwarfs - estimates for occurrence rate based on global detectability statistics. *Mon. Not. R. Astron. Soc* **441**, 1545–1569 (2014).

[16] Haario, H., Laine, M., Mira, A. & Saksman, E. Dram: Efficient adaptive mcmc. *Statistics and Computing* **16**, 339–354 (2006). URL `http://dx.doi.org/10.1007/s11222-006-9438-0`.

[17] Rajpaul, V., Aigrain, S. & Roberts, S. Ghost in the time series: no planet for Alpha Cen B. *Mon. Not. R. Astron. Soc* **456**, L6–L10 (2016).

[18] Bonfils, X. *et al.* The HARPS search for southern extra-solar planets. X. A m sin i = 11 $M_{\oplus}$ planet around the nearby spotted M dwarf GJ 674. *Astron. Astrophys.* **474**, 293–299 (2007).

[19] Barnes, J. R. *et al.* Precision radial velocities of 15 M5-M9 dwarfs. *Mon. Not. R. Astron. Soc* **439**, 3094–3113 (2014).

[20] Ofir, A. Optimizing the search for transiting planets in long time series. *Astron. Astrophys.* **561**, A138 (2014).

[21] Delfosse, X. *et al.* Accurate masses of very low mass stars. IV. Improved mass-luminosity relations. *Astron. Astrophys.* **364**, 217–224 (2000).

[22] Kopparapu, R. k. *et al.* The Inner Edge of the Habitable Zone for Synchronously Rotating Planets around Low-mass Stars Using General Circulation Models. *Astrophys. J.* **819**, 84 (2016).

[23] Reiners, A. & Basri, G. The moderate magnetic field of the flare star Proxima Centauri. *Astron. Astrophys.* **489**, L45–L48 (2008).

[24] Vidotto, A. A. *et al.* Effects of M dwarf magnetic fields on potentially habitable planets. *Astron. Astrophys.* **557**, A67 (2013).

[25] Zuluaga, J. I., Bustamante, S., Cuartas, P. A. & Hoyos, J. H. The Influence of Thermal Evolution in the Magnetic Protection of Terrestrial Planets. *Astrophys. J.* **770**, 23 (2013).

[26] Bolmont, E. *et al.* Water loss from Earth-sized planets in the habitable zones of ultracool dwarfs: Implications for the planets of TRAPPIST-1. *ArXiv e-prints* (2016).

[27] Tanaka, H., Takeuchi, T. & Ward, W. R. Three-Dimensional Interaction between a Planet and an Isothermal Gaseous Disk. I. Corotation and Lindblad Torques and Planet Migration. *Astrophys. J.* **565**, 1257–1274 (2002).

[28] Weidenschilling, S. J. Aerodynamics of solid bodies in the solar nebula. *Mon. Not. R. Astron. Soc* **180**, 57–70 (1977).

[29] Snellen, I. *et al.* Combining high-dispersion spectroscopy with high contrast imaging: Probing rocky planets around our nearest neighbors. *Astron. Astrophys.* **576**, A59 (2015).

[30] Lubin, P. A Roadmap to Interstellar Flight. *sub. to JBIS*, `arXiv:astro-ph/1604.01356` (2016)

Acknowledgements.

We thank Enrico Gerlach, Rachel Street and Ulf Seemann for their support to the science preparations. We thank Predrag Micakovic, Matthew M. Mutter (QMUL), Rob Ivison, Gaitee Hussain,

Ivo Saviane, Oana Sandu, Lars Lindberg Christensen, Richard Hook and the personnel at La Silla (ESO) for making the Pale Red Dot campaign possible. The authors acknowledge support from funding grants; Leverhulme Trust/UK RPG-2014-281 (HRAJ, GAE, MT), MINECO/Spain AYA-2014-54348-C3-1-R (PJA, CRL, ZMB, ER), MINECO/Spain ESP2014-54362-P (MJLG), MINECO/Spain AYA-2014-56637-C2-1-P(JLO, NM), J.A./Spain 2012-FQM1776 (JLO, NM), CATA-Basal/Chile PB06 Conicyt (JSJ), Fondecyt/Chile project #1161218 (JSJ), STFC/UK ST/M001008/1 (RPN, GALC, GAE), STFC/UK ST/L000776/1 (JB), ERC/EU Starting Grant #279347 (AR, LS, SVJ), DFG/Germany Research Grants RE 1664/9-2(AR), RE 1664/12-1(MZ), DFG/Germany Colloborative Research Center 963(CJM, SD), DFG/Germany Research Training Group 1351(LS), and NSF/USA grant AST-1313075 (ME). Based on observations made with ESO Telescopes at the La Silla Paranal Observatory under programmes 096.C-0082 and 191.C-0505. Observations were obtained with ASH2, which is supported by the Instituto de Astrofísica de Andalucía and Astroimagen company. This work makes use of observations from the LCOGT network. We acknowledge the effort of the UVES/M-dwarf and the HARPS/Geneva teams, which obtained a substantial amount of the data used in this work.

Author contributions. GAE led the PRD campaign, observing proposals and organized the manuscript. PJA led observing proposals, and organized and supported the IAA team through research grants. MT obtained the early signal detections and most Bayesian analyses. JSJ, JB, ZMB and HRAJ participated in the analyses and obtained activity measurements. Zaira M. Berdiñas also led observing proposals. HRAJ funded several co-authors via research grants. MK and ME provided the extracted UVES spectra, and RPB re-derived new RV measurements. CRL coordinated photometric follow-up campaigns. ER led the ASH2 team and related reductions (MJLG, IC, JLO, NM). YT led the LCOGT proposals, campaign and reductions. MZ obtained observations and performed analyses on HARPS and UVES spectra. AO analysed time-series and transit searches. JM, SVJ and AR analyzed stellar activity data. AR funded several co-authors via research grants. RPN, GALC, SJP, SD & BG did dynamical and studied the planet formation context. MK provided early access to time-series from the ASAS survey. CJM and LFS participated in the HARPS campaigns. All authors contributed to the preparation of observing proposals and the manuscript.

The authors declare that they do not have any competing financial interests.

Correspondence and requests for materials should be addressed to Guillem Anglada-Escudé, `g.anglada@qmul.ac.uk`

Table 1: Stellar properties, Keplerian parameters, and derived quantities. The estimates are the maximum *a posteriori* estimates and the uncertainties are expressed as 68% credibility intervals. We only provide an upper limit for the eccentricity (95% confidence level). Extended Data Table1 contains the list of all the model parameters.

Stellar properties	Value	Reference
Spectral type	M5.5V	[2]
$\mathrm{Mass}_*/\mathrm{Mass}_{\mathrm{Sun}}$	0.120 [0.105,0.135]	[21]
$\mathrm{Radius}_*/\mathrm{R}_{\mathrm{Sun}}$	0.141 [0.120,0.162]	[2]
$\mathrm{Luminosity}_*/\ \mathrm{L}_{\mathrm{Sun}}$	0.00155 [0.00149, 0.00161]	[2]
Effective temperature [K]	3050 [2950, 3150]	[2]
Rotation period [days]	~ 83	[3]
Habitable zone range [AU]	~ 0.0423 – 0.0816	[22]
Habitable zone periods [days]	~ 9.1–24.5	[22]
Keplerian fit	Proxima b	
Period [days]	11.186 [11.184, 11.187]	
Doppler amplitude [ms^{-1}]	1.38 [1.17, 1.59]	
Eccentricity [-]	$<$0.35	
Mean longitude $\lambda = \omega + M_0$ [deg]	110 [102, 118]	
Argument of periastron w_0 [deg]	310 [0,360]	
Statistics summary		
Frequentist false alarm probability	7×10^{-8}	
Bayesian odds in favour $\mathrm{B}_1/\mathrm{B}_0$	2.1×10^7	
UVES Jitter [ms^{-1}]	1.69 [1.22, 2.33]	
HARPS pre-2016 Jitter [ms^{-1}]	1.76 [1.22, 2.36]	
HARPS PRD Jitter [ms^{-1}]	1.14 [0.57, 1.84]	
Derived quantities		
Orbital semi-major axis a [AU]	0.0485 [0.0434, 0.0526]	
Minimum mass $m_p \sin i$ [$\mathrm{M}_\oplus$]	1.27 [1.10, 1.46]	
Eq. black body temperature [K]	234 [220, 240]	
Irradiance compared to Earth's	65%	
Geometric probability of transit	$\sim$1.5%	
Transit depth (Earth-like density)	$\sim$0.5%	

Methods

1 Statistical frameworks and tools

The analyses of time-series including radial velocities and activity indices were performed by frequentist and Bayesian methods. In all cases, significances were assessed using model comparisons by performing global multi-parametric fits to the data. Here we provide a minimal overview of the methods and assumptions used throughout the paper.

1.1 Bayesian statistical analyses.

The analyses of the radial velocity data were performed by applying posterior sampling algorithms called Markov chain Monte Carlo (MCMC) methods. We used the adaptive Metropolis algorithm[31] that has previously been applied to such radial velocity data sets.[15,32] This algorithm is simply a generalised version of the common Metropolis-Hastings algorithm[33,34] that adapts to the posterior density based on the previous members of the chain.

Likelihood functions and posterior densities of models with periodic signals are highly multi-modal (i.e. peaks in periodograms). For this reason, in our Bayesian signal searches we applied the delayed rejection adaptive Metropolis (DRAM) method,[16] that enables efficient jumping of the chain between multiple modes by postponing the rejection of a proposed parameter vector by first attempting to find a better value in its vicinity. For every given model, we performed several posterior samplings with different initial values to ensure convergence to a unique solution. When we identified two or more significant maxima in the posterior, we typically performed several additional samplings with initial states close to those maxima. This enabled us to evaluate all of their relative significances in a consistent manner. We estimated the marginal likelihoods and the corresponding Bayesian *evidence ratios* of different models by using a simple method.[35] A more detailed description of these methods can be found in elsewhere.[36]

1.2 Statistical models : Doppler model and likelihood function.

Assuming radial velocity measurements $m_{i,\mathrm{INS}}$ at some instant t_i and instrument INS, the likelihood function of the observations (probability of the data given a model) is given by

$$L = \prod_{\mathrm{INS}} \prod_{i} l_{i,\mathrm{INS}} \tag{1}$$

$$l_{i,\mathrm{INS}} = \frac{1}{\sqrt{2\pi\,(\sigma_i^2 + \sigma_{\mathrm{INS}}^2)}} \exp\left\{ -\frac{1}{2}\,\frac{\epsilon_{i,\mathrm{INS}}^2}{\sigma_i^2 + \sigma_{\mathrm{INS}}^2} \right\}, \tag{2}$$

$$\epsilon_{i,\mathrm{INS}} = m_{i,\mathrm{INS}} - \left\{ \gamma_{\mathrm{INS}} + \dot{\gamma}\Delta t_i + \kappa(\Delta t_i) + \mathrm{MA}_{i,\mathrm{INS}} + \mathrm{A}_{i,\mathrm{INS}} \right\}, \tag{3}$$

$$\Delta t_i = t_i - t_0 \tag{4}$$

where t_0 is some reference epoch. This reference epoch can be arbitrarily chosen, often as the beginning of the time-series or a mid-point of the observing campaigns. The other terms are:

- $\epsilon_{i,\mathrm{INS}}$ are the residuals to a fit. We assume that each $\epsilon_{i,\mathrm{INS}}$ is a Gaussian random variable with a zero mean and a variance of $\sigma_i^2 + \sigma_{\mathrm{INS}}^2$, where σ_i^2 is the reported uncertainty of the i-th measurement and σ_{INS}^2 is the *jitter parameter* and represents the excess white noise not included in σ_i^2.

- γ_{INS} is the *zero-point velocity* of each instrument. Each INS can have a different zero-point depending on how the radial velocities are measured and how the wavelengths are calibrated.

- $\dot{\gamma}$ is a *linear trend parameter* caused by a long term acceleration.

- The term $\kappa(\Delta t_i)$ is the superposition of k Keplerian signals evaluated at Δt_i. Each Keplerian signal depends on five parameters: the *orbital period* P_p, *semi-amplitude* of the signal K_p, mean anomaly $M_{0,p}$, which represents the phase of the orbit with respect to the periastron of the orbit at t_0, *orbital eccentricity* e_p that goes from 0 (circular orbit) to 1 (unbound parabolic orbit), and the *argument of periastron* ω_p, which is the angle on the orbital plane with respect to the plane of the sky at which the star goes through the periastron of its orbit (the planet's periastron is at $\omega_p + 180$ deg). Detailed definitions of the parameters can be found elsewhere.[37]

- The Moving Average term

$$\mathrm{MA}_{i,\mathrm{INS}} = \phi_{\mathrm{INS}} \exp\left\{\frac{t_{i-1} - t_i}{\tau_{\mathrm{INS}}}\right\} \epsilon_{i-1,\mathrm{INS}} \tag{5}$$

  is a simple parameterization of possible correlated noise that depends on the residual of the previous measurement $\epsilon_{i-1,\mathrm{INS}}$. As for the other parameters related to noise in our model, we assume that the parameters of the MA function depend on the instrument; for example the different wavelength ranges used will cause different properties of the instrumental systematic noise. Keplerian and other physical processes also introduce correlations into the data, therefore some degree of degeneracy between the MA terms and the signals of interest is expected. As a result, including a MA term always produces more conservative significance estimates than a model with uncorrelated random noise only. The MA model is implemented through a coefficient ϕ_{INS} and a time-scale τ_{INS}. ϕ_{INS} quantifies the strength of the correlation between the i and $i-1$ measurements. It is bound between -1 and 1 to guarantee that the process is stationary (i.e. the contribution of the MA term does not arbitrarily grow over time). The exponential smoothing is used to decrease the strength of the correlation exponentially as the difference $t_i - t_{i-1}$ increases.[38]

- Linear correlations with activity indices can also be included in the model in the following manner,

$$\mathrm{A}_{i,\mathrm{INS}} = \sum_{\xi} C_{\xi,\mathrm{INS}}\ \xi_{i,\mathrm{INS}} \tag{6}$$

  where ξ runs over all the activity indices used to model each INS dataset (e.g. m_2, m_3, S-index, etc. whose description is provided below). To avoid any confusion with other discussions about correlations, we call these $C_{\xi,\mathrm{INS}}$ *activity coefficients*. Note that each activity

coefficient $C_{\xi,\mathrm{INS}}$ is associated to one activity index (ξ_i) obtained simultaneously with the i-th radial velocity measurement (e.g. chromospheric emission from the H_α line, second moment of the mean-line profile, interpolated photometric flux, etc.). When fitting a model to the data, an activity coefficient significantly different from 0 indicates evidence of Doppler variability correlated with the corresponding activity index. Formally speaking, these $C_{\xi,\mathrm{INS}}$ correspond to the coefficient of the first order Taylor expansion of a physical model for the apparent radial velocities as a function of the activity indices and other physical properties of the star.

A simplified version of the same likelihood model is used when analyzing time-series of activity indices. That is, when searching for periodicities in series other than Doppler measurements, the model will consist of the γ_{INS} zero-points, a linear trend term $\dot{\gamma}\Delta t_i$, and a sum of n sinusoids

$$\hat{\kappa}(t_i,\vec{\theta}) \;=\; \sum_{k}^{n}\left(A_k \sin\frac{2\pi\Delta t_i}{P_k} + B_k\cos\frac{2\pi\Delta t_i}{P_k}\right) \tag{7}$$

where each k-th sinusoid has three parameters A_k, B_k, and P_k instead of the five Keplerian ones. Except for the period parameters and the jitter terms, this model is linear with all the other parameters, which allows a relatively quick computation of the likelihood-ratio periodograms.

1.3 Bayesian prior choices.

As in any Bayesian analysis, the prior densities of the model parameters have to be selected in a suitable manner (for example see[39]). We used uniform and uninformative distributions for most of the parameters apart from a few, possibly significant, exceptions. First, as we used a parameter $l = \ln P$ in the MCMC samplings instead of the period P directly, the uniform prior density $\pi(l) = c$ for all $l \in [\ln T_0, \ln T_{\max}]$, where T_0 and $T_{\max}$ are some minimum and maximum periods, does not correspond to a uniform prior in P. Instead, this prior corresponds to a period prior such that $\pi(P) \propto P^{-1}$.[40] We made this choice because the period can be considered a "scale parameter" for which an uninformative prior is one that is uniform in $\ln P$.[41] We selected the parameter space of the period such that $T_0 = 1$ day and $T_{\max} = T_{\mathrm{obs}}$, where T_{obs} is the baseline of the combined data.

For the semi amplitude parameter K, we used a $\pi(K) = c$ for all $K \in [0, K_{\max}]$, where $K_{\max}$ was selected as $K_{\max} = 10$ ms^{-1} because the RMSs of the Doppler series did not exceed 3 ms^{-1} in any of the sets. Following previous works,[40,42] we chose the prior for the orbital eccentricities as $\pi(e) \propto \mathcal{N}(0, \Sigma_e^2)$, where e is bound between zero (circular orbit) and 1. We set this $\Sigma_e^2 = 0.3$ to penalize high eccentricities while keeping the option of high e if the data strongly favours it.

We also used an informative prior for the excess white noise parameter of σ_{INS} for each instrument. Based on analyses of a sample of M dwarfs,[15] this "stellar jitter" is typically very close to a value of 1 ms^{-1}. Thus, we used a prior such that $\pi(\sigma_l) \propto \mathcal{N}(\mu_\sigma, \sigma_\sigma^2)$ such that the parameters were selected as $\mu_\sigma = \sigma_\sigma = 1$ ms^{-1}. Uniform priors were used in all the activity coefficients $C_\xi \in [-C_{\xi,max}, C_{\xi,max}]$. For practical purposes, the time-series of all activity indices were mean subtracted and normalized to their RMS. This choice allows us to select the bounds of the activity coefficients for the renormalized time-series as $\hat{C}_{\xi,max} = 3$ ms^{-1}, so that adding correlation terms

does not dramatically increase the RMS of the Doppler time-series over the initially measured RMS of < 3 ms^{-1} (same argument as for the prior on K). This renormalization is automatically applied by our codes at initialization.

1.4 Search for periodicities and significances in a frequentist framework.

Periodograms are plots representing a figure-of-merit derived from a fit against the period of a newly proposed signal. In the case of unevenly sampled data, a very popular periodogram is the Lomb-Scargle periodogram (or LS)[43,44] and its variants like the Floating-mean periodogram[45] or the F-ratio periodogram.[46] In this work we use likelihood ratio periodograms, which represent the improvement of the likelihood statistic when adding a new sinusoidal signal to the model. Due to intrinsic non-linearities in the Keplerian/RV modelling, optimizing the likelihood statistic is more computationally intensive than the classic LS-like periodograms[45,47]). On the other hand the likelihood function is a more general and well-behaved statistic which, for example, allows for the optimisation of the noise parameters (e.g. *jitter*, and fit correlated noise models at the signal search level). Once the maximum likelihood of a model with one additional planet is found (highest peak in the periodogram), its false-alarm probability can then be easily computed.[48,49] In general, a false-alarm probability of 1% is needed to claim hints of variability, and a value below 0.1% is considered necessary to claim a significant detection.

2 Spectroscopic datasets

2.1 New reduction of the UVES M-dwarf programme data.

Between 2000 and 2008, Proxima was observed in the framework of a precision RV survey of M dwarfs in search for extrasolar planets with the Ultraviolet and Visual Echelle Spectrograph (UVES) installed in the Very Large Telescope (VLT) unit 2 (UT2). To attain high-precision RV measurements, UVES was self-calibrated with its iodine gas absorption cell operated at a temperature of 70° C. The image slicer $\#3$ was chosen which redistributes the light from a $1'' \times 1''$ aperture along the chosen $0.3''$ wide slit. In this way, a resolving power of $R = 100,000 - 120,000$ was attained. At the selected central wavelength of 600 nm, the useful spectral range containing iodine (I_2) absorption lines ($\approx 500 - 600$ nm) falls entirely on the better quality detector of the mosaic of two $4K \times 2$K CCDs. More details can be found in the several papers from the UVES survey.[9,45,50]

The extracted UVES spectra include 241 observations taken through the Iodine cell, three template (no Iodine) shots of Proxima, and three spectra of the rapidly rotating B star HR 5987 taken through the Iodine cell as well, and almost consecutive to the three template shots. The B star has a smooth spectrum devoid of spectral features and it was used to calibrate the three template observations of the target. Ten of the Iodine observations of Proxima were eliminated due to low exposure levels. The remaining 231 iodine shots of Proxima were taken on 77 nights, typically 3 consecutive shots per night.

The first steps in the process of I_2 calibrated data consists of constructing the high signal to noise

template spectrum of the star without iodine: 1) a custom model of the UVES instrumental profile is generated based on the observations of the B star by forward modeling the observations using a higher-resolution ($R = 700,000 - 1,000,000$) template spectrum of the I_2 cell obtained with the McMath Fourier Transform Spectrometer (FTS) on Kitt Peak, 2) the three template observations of Proxima are then co-added and filtered for outliers, and 3) based on the instrument profile model and wavelength solution derived from the three B star observations, the template is deconvolved with our standard software.[10] After the creation of the stellar template, the 231 iodine observations of Proxima were then run through our standard precision velocity code.[8] The resulting standard deviation of the 231 un-binned observations is 2.58 ms^{-1}, and the standard deviation of the 77 nightly binned observations is 2.30 ms^{-1}, which already suggests an improvement compared to the 3.11 ms^{-1} reported in the original UVES survey reports.[50] All the UVES spectra (raw) are publicly available in their reduced form via ESO's archive at `http://archive.eso.org/cms.html`. Extracted spectra are not produced for this mode of UVES operation, but they are available upon request.

2.2 HARPS GTO.

The initial HARPS-Guaranteed Time Observations programme was led by Michel Mayor (ESO ID : 072.C-0488). 19 spectra were obtained between May 2005 and July 2008. The typical integration time ranges between 450 and 900 s.

2.3 HARPS M-dwarfs.

Led by X. Bonfils and collaborators, it consists of ESO programmes 082.C-0718 and 183.C-0437. It produced 8 and 46 measurements respectively with integration times of 900 s in almost all cases.[53]

2.4 HARPS high-cadence.

This program consisted of two 10 night runs (May 2013, and Dec 2013, ESO ID: 191.C-0505) and was led and executed by several authors of this paper. Proxima was observed on two runs

- May 2013 - 143 spectra obtained in three consecutive nights between May 4th and May 7th and 25 additional spectra between May 7th and May 16th with exposure times of 900 s.
- Dec 2013 -23 spectra obtained between Dec 30th and Jan 10th 2014 also with 900 s exposure times.

For simplicity in the presentation of the data and analyses, all HARPS data obtained prior to 2016 (HARPS GTO, HARPS M-dwarfs, and HARPS high-cadence) are integrated in the so-called HARPS pre-2016 set. The long-term Doppler variability and sparse sampling makes the detection of the Doppler signal more challenging in such a consolidated set than, for example, separating it into subsets of contiguous nights. The latter strategy, however, necessarily requires more parameters (offsets, jitter terms, correlated noise parameters) and arbitrary choices on the sets to be used, producing strong degeneracies and aliasing ambiguities in the determination of the favoured solution

(11.2-d was typically favoured, but alternative periods caused by a non-trivial window function at 13.6-d, 18.3-d were also found to be possible). The data taken in 2016 exclusively corresponds to the new campaign specifically designed to address the sampling issues.

2.5 HARPS : Pale Red Dot campaign.

PRD was executed between Jan 18th and March 30th, 2016. Few nights interruptions were anticipated to allow for technical work and other time-critical observations with HARPS. Of the 60 scheduled epochs, we obtained 56 spectra in 54 nights (two spectra were obtained in two of those nights). Integration times were set to 1200 s, and observations were always obtained at the very end of each night. All the HARPS spectra (raw, extracted and calibrated frames) are publicly available in their reduced form via ESO's archive at `http://archive.eso.org/cms.html`.

3 Spectroscopic indices

Stellar activity can be traced by features in the stellar spectrum. For example, changes in the line-profile shapes (symmetry and width) have been associated to spurious Doppler shifts.[18,51] Chromospheric emission lines are tracers of spurious Doppler variability in the Sun and they are expected to behave similarly for other stars.[52] We describe here the indices measured and used in our analyses.

3.1 Measurements of the mean spectral line profiles.

The HARPS Data Reduction Software provides two measurements of the mean-line profile shapes derived from the cross-correlation function (CCF) of the stellar spectrum with a binary mask. These are called the bisector span (or BIS) and full-width-at-half-maximum (or FWHM) of the CCF.[53] For very late type stars like Proxima, all spectral lines are blended producing a non-trivial shape of the CCF, and thus the interpretation of the usual line-shape measurements is not nearly as reliable as in earlier type stars. We applied the Least-Squares Deconvolution (LSD) technique[54] to obtain a more accurate estimate of the spectral mean line profile. This profile is generated from the convolution of a kernel, which is a model spectrum of line positions and intensities, with the observed spectrum. A description of our implementation of the procedure, applied specifically to crowded M-dwarf spectra is described in.[55] The LSD profile can be interpreted as a probability function distribution that can then be characterized by its central moments.[56] We computed the second (m_2) and third (m_3) central moments of each LSD-profile of each observation. More details of these indices and how they compare to other standard HARPS cross-correlation measurements can be found in.[11] To eliminate the correlation of the profile moments with the slope of the spectral energy distribution,[11] we corrected the SED and blaze function to match the same spectral energy distribution of the highest S/N observation obtained with HARPS. Uncertainties were obtained using an empirical procedure as follows: we derived all the m_2 and m_3 measurements of the high-cadence night of May 7th 2013 and fitted a polynomial to each time-series. The standard deviation of the residuals to that fit was then assumed to be the expected uncertainty for a S/N$\sim$20 (at reference echelle aperture number

60), which was the typical value for that night's observations. All other errors were then obtained by scaling this standard deviation by a factor of $\frac{20}{S/N_{\rm obs}}$ for each observation.

3.2 Chromospheric indices.

Chromospheric emission lines are tracers of spurious Doppler variability in the Sun and they are expected to behave similarly for other stars.[52] We describe here the indices computed and used in our analyses.

3.3 Chromospheric CaII H+K S-index.

We calculated the CaII H+K fluxes following standard procedures,[57,58] both the PRD data and the pre-2016 data were treated the same. Uncertainties were calculated from the quadrature sum of the variance in the data used within each bandpass.

3.4 Chromospheric H_α emission.

This index was measured in a similar way to the S-indices, such that we summed the fluxes in the center of the lines, calculated to be 6562.808 Å, this time utilising square bandpasses of 0.678 Å not triangular shapes, and those were normalized to the summed fluxes of two square continuum band regions surrounding each of the lines in the time series. The continuum square bandpasses were centered at 6550.870 Å and 6580.309 Å and had widths of 10.75 Å and 8.75 Å, respectively. Again the uncertainties were calculated from the quadrature sum of the variance of the data within the bandpasses.

4 Photometric datasets

4.1 Astrograph Southern Hemisphere II.

The ASH2 (Astrograph for the South Hemisphere II) telescope is a 40 cm robotic telescope with a CCD camera STL11000 2.7K x 4K, and a field-of-view (FOV) of 54 x 82 arcmin. Observations were obtained in two narrow-band filters centered on H_α and SII lines, respectively (H_α is centred on 656 nm, SII is centered on 672 nm, and both filters have a Gaussian-like transmission with a FWHM of 12 nm). The telescope is at SPACEOBS (San Pedro de Atacama Celestial Explorations Observatory), at 2450 m above sea level, located in the northern Atacama Desert, in Chile. This telescope is managed and supported by the Instituto de Astrofísica de Andalucía (Spain). During the present work, only subframes with 40% of the total field of view were used, resulting in a useful FOV of 21.6 $\times$ 32.8 arcmin. Approximately 20 images in each band of 100 s of exposure time were obtained per night. In total, 66 epochs of about 100 min each were obtained during this campaign. The number of images collected per night was increased during the second part of the campaign (until about 40 images in each filter per night).

All CCD measurements were obtained by the method of synthetic aperture photometry using a 2 $\times$ 2 binning. Each CCD frame was corrected in a standard way for dark and flat-fielding. Different aperture sizes were also tested in order to choose the best one for our observations. A number of nearby and relatively bright stars within the frames were selected as check stars in order to choose the best ones to be used as comparison stars. After checking their stability, C2=HD 126625 and C8=TYC 9010-3029-1, were selected as main comparison stars.

The basic photometric data were computed as magnitude differences in SII and H_α filters for Var-X and C2-X, with Var=Prox Cen and X=(C2+C8)/2. Typical uncertainties of each individual data point are about 6.0 mmag, for both SII and H_α filters. This usually leads to error-bars of about 1.3 mmag in the determination of the mean levels of each epoch, assuming 20 points per night once occasional strong activity episodes (such as flares) are removed for the analysis of periodicities. For the analyses, these magnitudes were transformed to relative flux measurements normalized to the mean flux over the campaign.

4.2 Las Cumbres Observatory Global Telescope network.

The Las Cumbres Observatory (LCOGT) is an organization dedicated to time-domain astronomy.[13] To facilitate this, LCOGT operates a homogeneous network of 1 m and 2 m telescopes on multiple sites around the world. The telescopes are controlled by a single robotic scheduler, capable of orchestrating complex responsive observing programs, using the entire network to provide uninterrupted observations of any astronomical target of interest. Each site hosts between one to three telescopes, which are configured for imaging and spectroscopy. The telescopes are equipped with identical instruments and filters, which allows for 'network redundancy'. This means that observations can be seamlessly shifted to alternate sites at any time if the scientific program requires it, or in the event of poor weather.

Observations for the PRD campaign were obtained on the 1 m network every 24 hours in the B and V bands with the Sinistro (4K x 4K Fairchild CCD486) cameras, which have a pixel scale of 0.38 arcsec and a FOV of 27 x 27 arcminutes. In addition, B and V observations were taken every 12 hours with the SBIG (4K x 4K Kodak KAF-6303E CCD) cameras, with a pixel scale of 0.46 arcsec and a FOV of 16 x 16 arcminutes. Exposure times ranged between 15 and 40 s and a total of 488 photometrically useful images were obtained during the campaign.

The photometric measurements were performed using aperture photometry with AstroImageJ[59] and DEFOT.[60] The aperture sizes were optimized during the analysis with the aim of minimizing measurement noise. Proxima Centauri and two non-variable comparison stars were identified in a reference image and used to construct the detrended light curves. As with the ASH2 curves, the LCOGT differential magnitudes were transformed to normalized flux to facilitate interpretation and later analyses (see Figure 3 in main article).

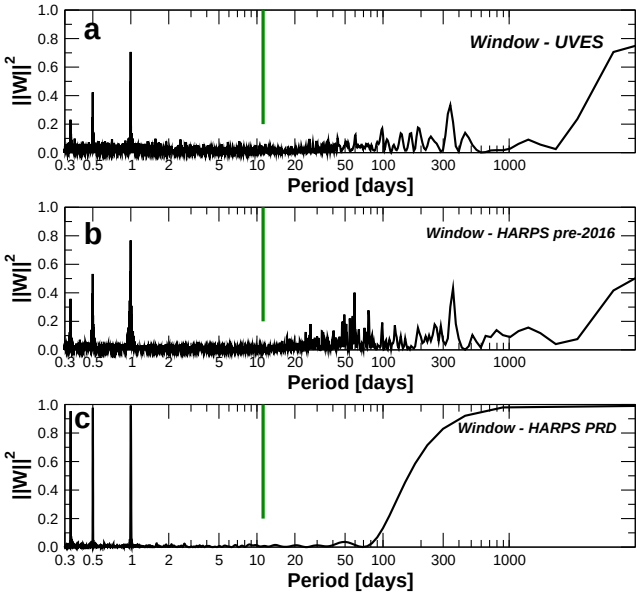

Extended Data Figure 1: **Window function.** Window function of the UVES (panel a), HARPS pre-2016(panel b) and HARPS PRD (panel c) datasets. The same window function applies to the time-series of Doppler and activity data. Peaks in the window function are periods at which aliases of infinite period signals would be expected.

5 Signals in time-series

In this section we present a homogeneous analysis of all the time-series (Doppler, activity and photometric ones) presented in this article. In all periodograms, the black curve represents the search for a first signal. If one first signal is identified, then a red curve represents the search for a second signal. In the few cases where a second signal is detected, a blue curve represents the search for a third signal. The period of Proxima b is marked with a green vertical line.

5.1 Module of the Window function.

We first present the so-called window function of the three sets under discussion. The window function is the Fourier transform of the sampling.[61] Its module shows the frequencies (or periods) where a signal with 0 frequency (or infinite period) would have its aliases. As shown in Extended Data Figure 1, both the UVES and HARPS PRD campaigns have a relatively clear window function between 1 and 360 days, meaning that peaks in periodograms can be interpreted in a very straightforward way (no aliasing ambiguities). For the UVES case, this happens because the measurements were uniformly spread over several years without severe clustering, producing only strong aliases at frequencies beating caused by the usual daily and yearly sampling (peaks at 360, 1, 0.5 and 0.33 days). The window of the PRD campaign is simpler, which is the result of a shorter timespan and the uniform sampling of the campaign. On the other hand, the HARPS pre-2016 window function (panel b in Extended Data Figure 1) contains numerous peaks between 1 and 360 days. This means that

signals (e.g. activity) in the range of a few hundred days will inject severe interference in the period domain of interest, and explains why this set is where the Doppler signal at 11.2 days is detected with less confidence (see Extended Data Figure 2).

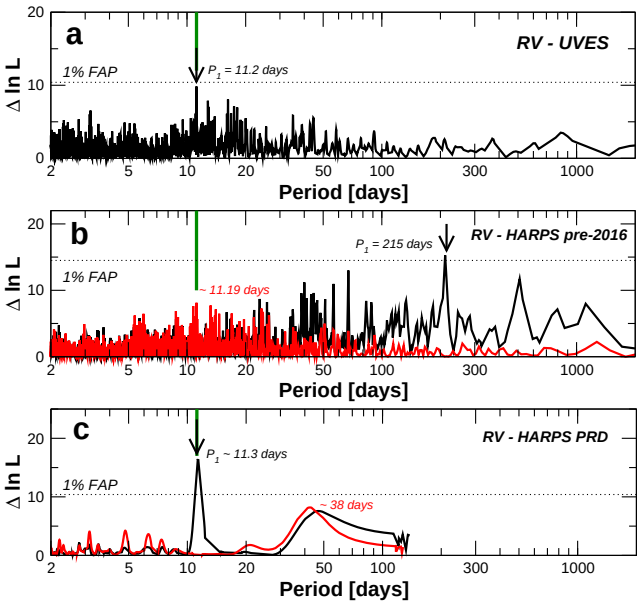

Extended Data Figure 2: **Signal searches on independent radial velocity datasets.** Likelihood-ratio periodograms searches on the RV measurements of the UVES (panel a), HARPS pre-2016 (panel b) and HARPS PRD (panel c) subsets. The periodogram with all three sets combined is shown in Figure 1 of the main manuscript. Black and red lines represent the searches for A first and a second signal respectively.

5.2 Radial velocities.

Here we present likelihood-ratio periodogram searches for signals in the three Doppler time-series separately (PRD, HARPS pre-2016, and UVES). They are analyzed in the same way as the activity indices to enable direct visual comparison. They differ from the ones presented in the main manuscript in the sense that they do not include MA terms and the signals are modelled as pure sinusoids to mirror the analysis of the other time-series as close as possible. The resulting periodograms are shown in Extended data Figure 2. A signal at 11.2 days was close to detection using UVES data-only. However, let us note that the signal was not clearly detectable using the Doppler measurements as provided by the UVES survey,[45] and it only became obvious when new Doppler measurements were re-derived using up-to-date Iodine codes (Section 2.1). The signal is weaker in the HARPS pre-2016 dataset, but it still appears as a possible second signal after modeling the longer term variability with a Keplerian at 200 days. Sub-sets of the HARPS pre-2106 data taken in consecutive nights (eg. HARPS high-cadence runs) also show strong evidence of the same signal. However splitting the data in subsets adds substantial complexity to the analysis and the results become quite sensitive to subjective choices (how to split the data and how to weight each subset). The combination UVES with all the HARPS pre-2016 (Figure 1, panel a) already produced a FAP of $\sim$1%, but a dedicated campaign was deemed necessary given the caveats with the sampling and activity related variability. The HARPS PRD campaign unambiguously identifies a signal with the

same ~ 11.2 days period. As discussed earlier, the combination of all the data results in a very high significance, which implies that the period, but also the amplitude and phase are consistent in all three sets.

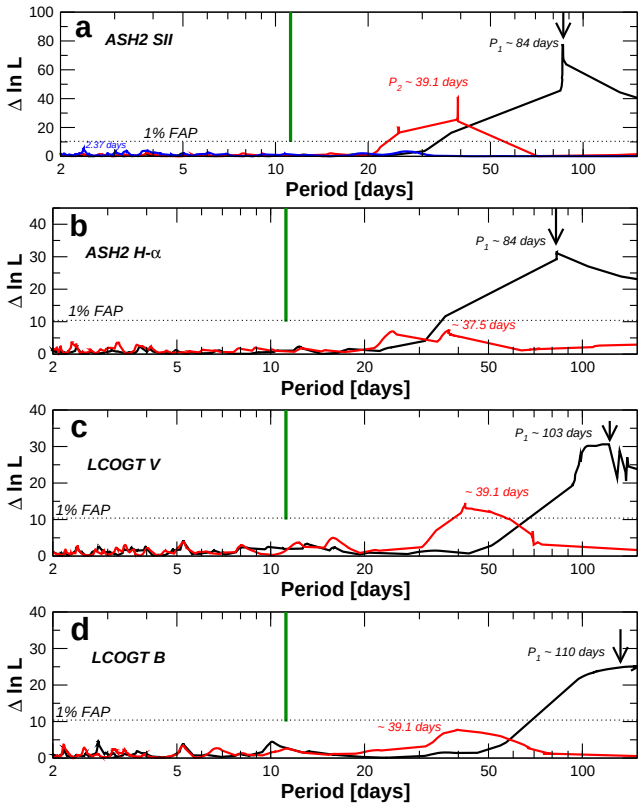

Extended Data Figure 3: **Signal searches on the photometry**. Likelihood-ratio periodograms searches for signals in each photometric ASH2 photometric band (panels a and b) and LCOGT bands (panels c and d). The two sinusoid fit to the ASH2 SII series ($P_1 = 84$ days, $P_2 = 39.1$ days), is used later to construct the FF′ model to test for correlations of the photometry with the RV data. Black, red and blue lines represent the search for a first, second and third signals respectively.

5.3 Photometry. Signals and calculation of the FF′ index.

The nightly average of the four photometric series was computed after removing the measurements clearly contaminated by flares (see Figure 3 in main manuscript). This produces 43 LCOGT epochs in the B and V bands (80 nights), and 66 ASH2 epochs in both SII and H_α bands (100 nights covered). The precision of each epoch was estimated using the internal dispersion within a given night. All four photometric series show evidence of a long period signal compatible with a photometric cycle at 83-d (likely rotation) reported before.[3] See periodograms in Extended data Figure 3.

In the presence of spots, it has been proposed that spurious variability should be linearly correlated with the value of the normalized flux of the star F, the derivative of the flux F′, and the product of FF′[62] in what is sometimes called the FF′ model. To include the photometry in the analysis of the Doppler data, we used the best model fit of the highest quality light curve (AHS2 SII, has the lowest post-fit scatter) to estimate F, F' and FF' at the instant of each PRD observation. The relation of F, F', and FF' to the Doppler variability is investigated later in the Bayesian analysis of the

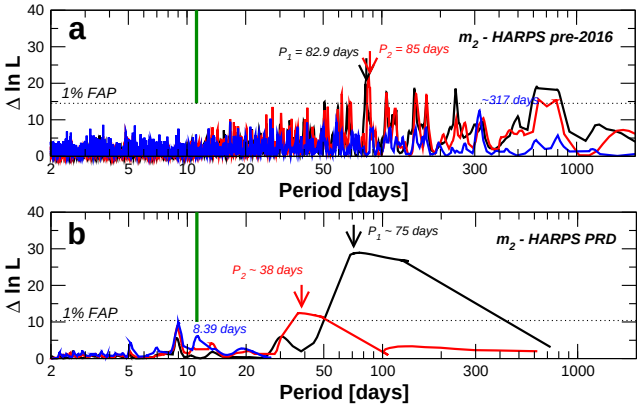

Extended Data Figure 4: **Signal searches on the width of the spectral lines.** Likelihood periodogram searches on the width of the mean spectral line as measured by m_2 for the HARPS pre-2016 (panel a) and HARPS PRD data (panel b). The signals in the HARPS pre-2016 data are comparable to the photometric period reported in the literature and the variability in the HARPS PRD run compares quite well to the photometric variability. Black, red and blue lines represent the search for a first, second and third signal respectively.

correlations.

5.4 Width of the mean spectral line as measured by m_2.

The m_2 measurement contains a strong variability that closely mirrors the measurements from the photometric time-series (see Figure 3 in the main manuscript). As in the photometry, the rotation period and its first harmonic (~ 40 days) are clearly detected in the PRD campaign (see Extended data Figure 4). This apparently good match needs to be verified on other stars as it might become a strong diagnostic for stellar activity in M-stars. The analysis of the HARPS pre-2016 also shows very strong evidence that m_2 is tracing the photometric rotation period of 83 days. The modelling of this HARPS pre-2016 requires a second sinusoid with $P_2 \sim 85$ days, which is peculiar given how close it is to P_1. We suspect this is caused by photospheric features on the surface changing over time.

5.5 Asymmetry of the mean spectral lines as monitored by m_3

The periodogram analysis of m_3 of the PRD run suggests a signal at 24 days which is close to twice the Doppler signal of the planet candidate (see Extended Data Figure 5). However, line asymmetries are expected to be directly correlated with Doppler signals, not at twice nor integer multiples of the Doppler period. In addition, the peak has a FAP$\sim$ 5% which makes it non-significantly different from white noise. When looking at the HARPS pre-2016 data, some strong beating is observed at 179 and 360 days, which is likely caused by a poorly sampled signal at that period or longer (magnetic cycle?), or some residual systematic effect (contamination by tellurics?). In summary, m_3 does not show evidence of any stable signal in the range of interest.

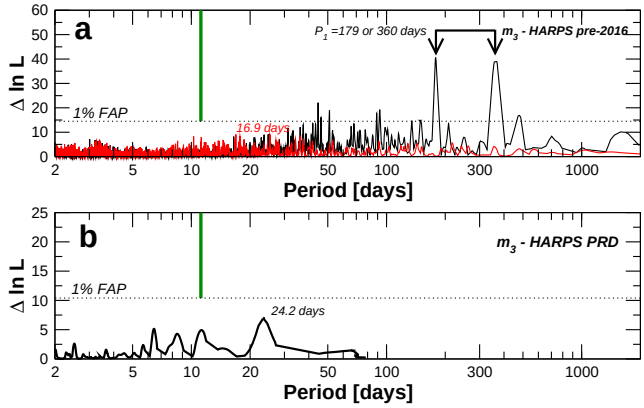

Extended Data Figure 5: **Signal searches on the assymetry of the spectral lines.** Likelihood periodogram searches on the line asymmetry as measured by m_3 from the HARPS pre-2016 (panel a) and HARPS PRD (panel b) datasets. A signal beating at $\sim$ 1 year and 1/2 year is detected in the HARPS pre-2016 data, possibly related to instrumental systematic effects or telluric contamination. No signals are detected above 1% threshold in the HARPS PRD campaign. Black and red lines represent the search for first and second signals respectively.

5.6 Signal searches in S-index.

While H_α[52] and other lines like the sodium doublet (NaD1 and NaD2)[63] have been shown to be the best tracers for activity on M-dwarfs, analyzing the time-series of the S-index is also useful because of its historical use in long term monitoring of main-sequence stars.[64] In Extended Data Figure 6 we show the likelihood ratio periodograms for the S-indices of the HARPS pre-2016 and PRD time-series. As can be seen, no signals were found around the 11 day period of the radial velocity signal, however two peaks were found close the 1% false alarm probability threshold with periods of $\sim$170 and 340 days. In order to further test the reality of these possible signals, we performed a Lomb-Scargle (LS) periodogram analysis[44] of the combined PRD and pre-2016 HARPS data. This test resulted in the marginal recovery of both the 170 and 340 day peaks seen in the likelihood periodograms, with no emerging peaks around the proposed 11 day Doppler signal. The LS tests revealed some weak evidence for a signal at much lower periods, $\sim$7 days and $\sim$30 days.

Given that there is evidence for significant peaks close to periods of 1 yr, its first harmonic, and the lunar period, we also analysed the window function of the time-series to check if there was evidence that these peaks are artefacts from the combination of the window function pattern interfering with a real long-period activity signal in the data. The dominant power in the window function is found to increase at periods greater than 100 days, with a forest of strong peaks found in that domain, in comparison to sub-100 day periods which is very flat, representing the noise floor of the time-series. This indicates that there is likely to be strong interference patterns from the sampling in this region, and that the signal in the radial velocity data is also not due to the sampling of the data. A similar study in the context of the HARPS M-dwarf program was also done on Proxima.[63] They compared several indices and finally decided to use the intensity of the chromospheric sodium

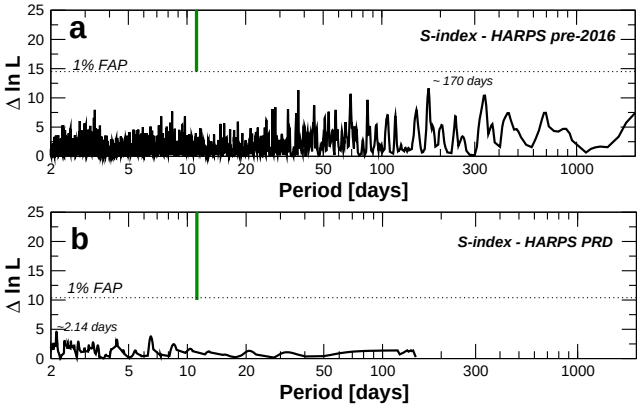

Extended Data Figure 6: **Signal searches on the chromospheric S-index.** Likelihood-ratio periodogram of S-index from the HARPS pre-2016 (panel a) and HARPS PRD (panel b) campaigns. No signals detected above 1% threshold.

doublet lines. They did not report any significant period at the time, but we suspect this was due to using fewer measurements, and not removing the frequent flaring events from the series, which also requires compilation of a number of observations to reliably identify outliers caused by flares.

5.7 Signal searches in H_α emission

Our likelihood-ratio periodograms for H_α (Extended Data Figure 7) only show low significance peaks in the 30-40 days period range. It is important to note that the analyses described above have been performed on multiple versions of the dataset, in the sense that we analysed the full dataset without removing measurements affected by flaring, then proceeded to reanalyse the activities by dropping data clearly following the flaring periods that Proxima went through when we observed the star. This allowed us to better understand the impact that flares and outliers have on signal interference in the activity indices. Although the distribution of peaks in periodograms changes somewhat depending on how stringent the cuts are, no emerging peaks were seen close to an 11 day period. Concerning UVES H_α measurements, our likelihood-ratio periodogram did not detect any significant signal.

5.8 Further tests on the signal.

It has been shown[65] that at least some of the ultraprecise photometric time-series measured by CoRot and Kepler space missions do not have a necessary property to be represented by a Fourier expansion: the underlying function, from which the observations are a sample, must be analytic. An algorithm introduced in the same paper can test this property and was applied to the PRD data. The result is that, contrary to the light curves aforementioned, claims that the underlying function is non-analytic does not hold with the information available. Though the null hypothesis cannot be definitively rejected, at least until more data is gathered, our results are consistent with the hypothesis that a

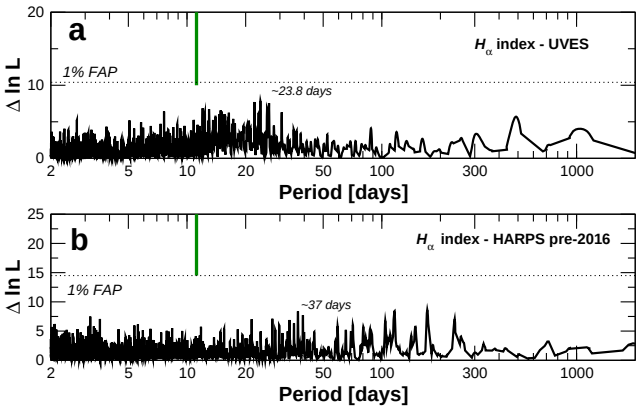

Extended Data Figure 7: **Signal searches on the spectroscopic H_α index** Likelihood-ratio periodogram searches of H_α intensity from the UVES (panel a), HARPS pre-2016 (panel b) and HARPS PRD (panel c) campaigns. No signals detected above 1% threshold.

harmonic component is present in the Doppler time-series.

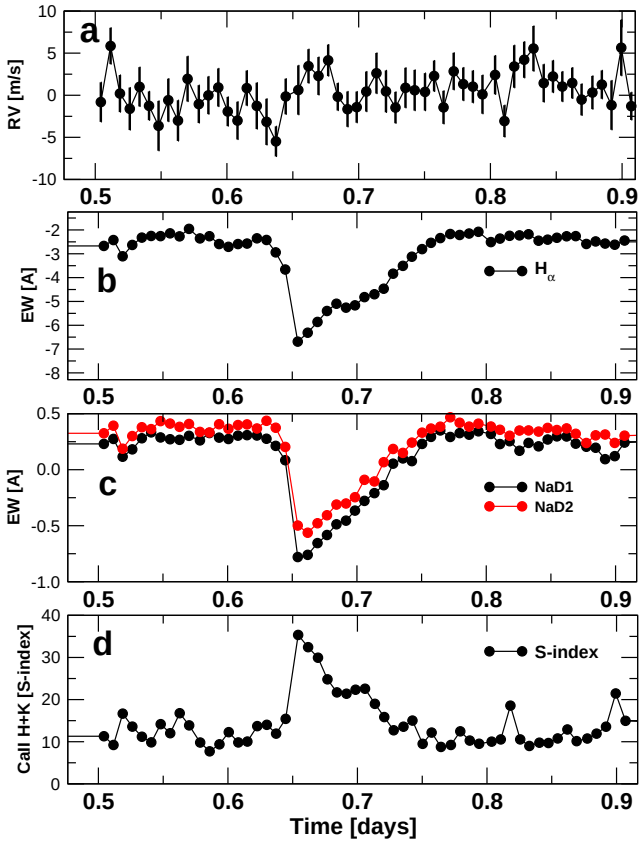

Extended Data Figure 8: **Radial velocities and chromospheric emission during a flare.** Radial velocities (panel a) and equivalent width measurements of the H_α (panel b), Na Doublet lines (panel c), and the S-index (panel d) as a function of time during a flare that occurred the night of May 5th, 2013. Time axis is days since JD=245417.0 days. No trace of the flare is observed on the RVs.

5.9 Flares and radial velocities.

Among the high-cadence data from May 2013 with HARPS, two strong flares are fully recorded. During these events, all chromospheric lines become prominent in emission, H_α being the one that best traces the characteristic time-dependence of flares observed on other stars and the Sun. The spectrum and impact of flares on the RVs will be described elsewhere in detail. Relevant to this study, we show th at the typical flares on Proxima do not produce correlated Doppler shifts (Extended Data Figure 8). This justifies the removal of obvious flaring events when investigating signals and correlations in the activity indices.

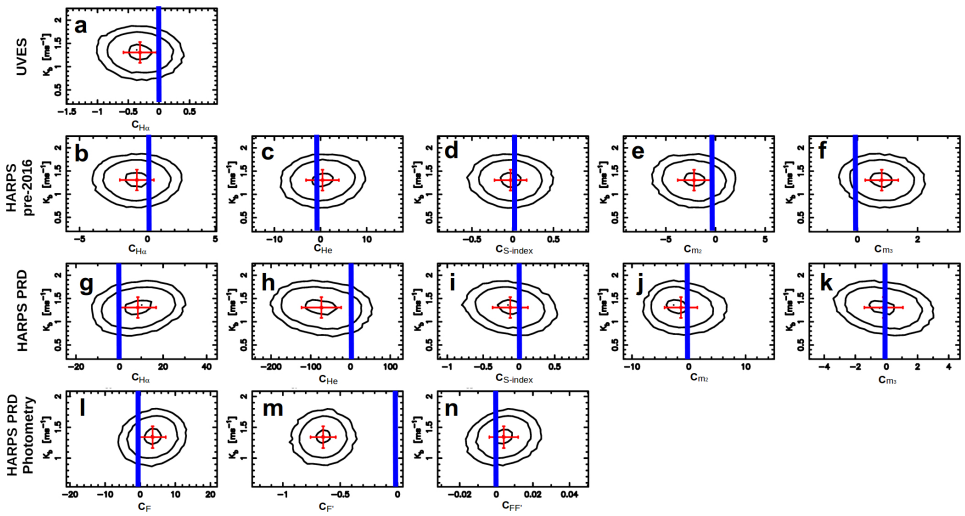

Extended Data Figure 9: **Probability distributions for the activity coefficients versus signal amplitude.** Marginalized posterior densities of the activity coefficients versus the semi-amplitude of the signal for UVES (panel a), HARPS pre-2016 (panels b,c,d,e,f), HARPS PRD campaign (panels g,h,i,j,k) and the photometric FF′ indices for the PRD campaign only (panels l, m, n). Each panel shows equiprobability contours containing 50%, 95%, and 99% of the probability density around the mean estimate, and the corresponding standard deviation of the marginalized distribution (1-σ) in red. The blue bar shows the zero value of each activity coefficient. Only $C_{F'}$ is found to be significantly different from zero.

6 Complete model and Bayesian analysis of the activity coefficients.

A global analysis including all the RVs and indices was performed to verify that the inclusion of correlations would reduce the model probability below the detection thresholds. Equivalently, the Doppler semi-amplitude would become consistent with zero if the Doppler signal was to be described by a linear correlation term. Panels in Extendent Data Figure 9 show marginalized distributions of linear correlation coefficients with the Doppler semi-amplitude K. Each subset is treated as a separate instrument and has its own zero-point, jitter and Moving Average term (coefficient) and its activity coefficients. In the final model, the time-scales of the Moving Average terms are fixed to ~ 10 days because they were not contrained within the prior bounds, thus compromising the convergence of the chains. The sets under consideration are

- **UVES** : 70 radial velocity measurements and corresponding H_α emission measurements.
- **HARPS pre-2016** : 90 radial velocity measurements obtained between 2002 and 2014 by several programmes and corresponding spectroscopic indices : m_2, m_3, S-index, and the intensities of the H_α and HeI lines as measured on each spectrum.

- **HARPS PRD** : 54 Doppler measurements obtained between Jan 18th-Mar 31st, 2016, and the same spectroscopic indices as for the HARPS pre-2016. The values of the F, F$'$ and FF$'$ indices were obtained by evaluating the best fit model to the ASH2 SII photometric series at the HARPS epochs (see Section 5.3).

An activity index is correlated with the RV measurements in a given set if the zero value of its activity coefficient is excluded from the 99% credibility interval. Extended Data Figure 9 shows the equiprobability contours containing 50%, 95%, and 99% of the probability density around the mean estimate, and the corresponding 1-σ uncertainties in red. Only the F' index (time derivative of the photometric variability) is significantly different from 0 at high confidence (Extended Data Figure 9, bottom row, panel m). Linking this correlation to a physical process requires further investigation. To ensure that such correlations are causally related, one needs a model of the process causing the signal in both the RV and the index, and in the case of the photometry one would need to simultaneously cover more stellar photometric periods to verify that the relation holds over time. Extended Data Table 1 contains a summary of all the free parameters in the model including activity coefficients for each dataset.

References

[31] Haario, H., Saksman, E. & Tamminen, J. –. *Bernouilli* **7**, 223 (2001).

[32] Tuomi, M. *et al.* Signals embedded in the radial velocity noise. Periodic variations in the τ Ceti velocities. *Astron. Astrophys.* **551**, A79 (2013).

[33] Metropolis, N., Rosenbluth, A., Rosenbluth, M., Teller, A. & Teller, E. Equations of State Calculations by Fast Computing Machines. *JChPh* **21**, 1087–192 (1953).

[34] Hastings, W. K. Monte carlo sampling methods using markov chains and their applications. *Biometrika* **57**, 97–109 (1970). URL `http://www.jstor.org/stable/2334940`.

[35] Newton, M. A. & Raftery, A. E. –. *JRSS B* **56**, 3– (1994).

[36] Tuomi, M. A new cold sub-Saturnian candidate planet orbiting GJ 221. *Mon. Not. R. Astron. Soc* **440**, L1–L5 (2014).

[37] Wright, J. T. & Howard, A. W. Efficient Fitting of Multiplanet Keplerian Models to Radial Velocity and Astrometry Data. *Astrophys. J. Suppl.* **182**, 205–215 (2009).

[38] Scargle, J. D. Studies in astronomical time series analysis. I - Modeling random processes in the time domain. *Astrophys. J. Suppl.* **45**, 1–71 (1981).

[39] Tuomi, M. Evidence for nine planets in the HD 10180 system. *Astron. Astrophys.* **543**, A52 (2012).

[40] Tuomi, M. & Anglada-Escudé, G. Up to four planets around the M dwarf GJ 163. Sensitivity of Bayesian planet detection criteria to prior choice. *Astron. Astrophys.* **556**, A111 (2013).

[41] Berger, J. O. *Statistical Decision Theory and Bayesian Analysis* (Springer, 1980).

[42] Anglada-Escudé, G. *et al.* A dynamically-packed planetary system around GJ 667C with three super-Earths in its habitable zone. *Astron. Astrophys.* **556**, A126 (2013).

[43] Lomb, N. R. Least-squares frequency analysis of unequally spaced data. *AP&SS* **39**, 447–462 (1976).

[44] Scargle, J. D. Studies in astronomical time series analysis. II - Statistical aspects of spectral analysis of unevenly spaced data. *Astrophys. J.* **263**, 835–853 (1982).

[45] Zechmeister, M., Kürster, M. & Endl, M. The M dwarf planet search programme at the ESO VLT + UVES. A search for terrestrial planets in the habitable zone of M dwarfs. *Astron. Astrophys.* **505**, 859–871 (2009).

[46] Cumming, A. Detectability of extrasolar planets in radial velocity surveys. *Mon. Not. R. Astron. Soc* **354**, 1165–1176 (2004).

[47] Ferraz-Mello, S. Estimation of Periods from Unequally Spaced Observations. *Astron J.* **86**, 619 (1981).

[48] Baluev, R. V. Accounting for velocity jitter in planet search surveys. *Mon. Not. R. Astron. Soc* **393**, 969–978 (2009).

[49] Baluev, R. V. The impact of red noise in radial velocity planet searches: only three planets orbiting GJ 581? *Mon. Not. R. Astron. Soc* 420 (2012).

[50] Endl, M. & Kürster, M. Toward detection of terrestrial planets in the habitable zone of our closest neighbor: proxima Centauri. *Astron. Astrophys.* **488**, 1149–1153 (2008).

[51] Queloz, D. *et al.* No planet for HD 166435. *Astron. Astrophys.* **379**, 279–287 (2001).

[52] Robertson, P., Mahadevan, S., Endl, M. & Roy, A. Stellar activity masquerading as planets in the habitable zone of the M dwarf Gliese 581. *Science* **345**, 440–444 (2014).

[53] Bonfils, X. *et al.* The HARPS search for southern extra-solar planets. XXXI. The M-dwarf sample. *Astron. Astrophys.* **549**, A109 (2013).

[54] Donati, J.-F. & Brown, S. F. Zeeman-Doppler imaging of active stars. V. Sensitivity of maximum entropy magnetic maps to field orientation. *Astron. Astrophys.* **326**, 1135–1142 (1997).

[55] Barnes, J. R. *et al.* Red Optical Planet Survey: a new search for habitable earths in the southern sky. *Mon. Not. R. Astron. Soc* **424**, 591–604 (2012).

[56] Press, W. H., Teukolsky, S. A., Vetterling, W. T. & Flannery, B. P. *Numerical recipes in FORTRAN. The art of scientific computing* (Cambridge: University Press, —c1992, 2nd ed., 1992).

[57] Jenkins, J. S. *et al.* An activity catalogue of southern stars. *Mon. Not. R. Astron. Soc* **372**, 163–173 (2006).

[58] Jenkins, J. S. *et al.* Metallicities and activities of southern stars. *Astron. Astrophys.* **485**, 571–584 (2008).

[59] Collins, K. A., Kielkopf, J. F. & Stassun, K. G. AstroImageJ: Image Processing and Photometric Extraction for Ultra-Precise Astronomical Light Curves. *ArXiv e-prints* (2016).

[60] Southworth, J. *et al.* High-precision photometry by telescope defocussing - VI. WASP-24, WASP-25 and WASP-26. *Mon. Not. R. Astron. Soc* **444**, 776–789 (2014).

[61] Dawson, R. I. & Fabrycky, D. C. Radial Velocity Planets De-aliased: A New, Short Period for Super-Earth 55 Cnc e. *Astrophys. J.* **722**, 937–953 (2010).

[62] Aigrain, S., Pont, F. & Zucker, S. A simple method to estimate radial velocity variations due to stellar activity using photometry. *Mon. Not. R. Astron. Soc* **419**, 3147–3158 (2012).

[63] Gomes da Silva, J. *et al.* Long-term magnetic activity of a sample of M-dwarf stars from the HARPS program . II. Activity and radial velocity. *Astron. Astrophys.* **541**, A9 (2012).

[64] Baliunas, S. L. *et al.* Chromospheric variations in main-sequence stars. *Astrophys. J.* **438**, 269–287 (1995).

[65] Pascual-Granado, J., Garrido, R. & Suárez, J. C. Limits in the application of harmonic analysis to pulsating stars. *Astron. Astrophys.* **581**, A89 (2015).

Extended Data Table 1: **Complete set of model parameters**. The definition of all the parameters is given in Section 1 of the methods. The values are the maximum *a posteriori* estimates and the uncertainties are expressed as 68% credibility intervals. The reference epoch for this solution is Julian Date $t_0 = 2451634.73146$ days, which corresponds to the first UVES epoch. *Units of the activity coefficients are ms^{-1}divided by the units of each activity index.

Parameter	Mean [68% c.i.]	Units
Period	11.186 [11.184, 11.187]	days
Doppler Amplitude	1.38 [1.17, 1.59]	ms^{-1}
Eccentricity	$<$0.35	–
Mean Longitude	110 [102, 118]	deg
Argument of periastron	310 [-]	deg
Secular acceleration	0.086 [-0.223, 0.395]	$\mathrm{ms}^{-1}\mathrm{yr}^{-1}$
Noise parameters		
σ_{HARPS}	1.76 [1.22, 2.36]	ms^{-1}
σ_{PRD}	1.14 [0.57, 1.84]	ms^{-1}
σ_{UVES}	1.69 [1.22, 2.33]	ms^{-1}
ϕ_{HARPS}	0.93 [0.46, 1]	ms^{-1}
ϕ_{PRD}	0.51 [-0.63, 1]	ms^{-1}
ϕ_{UVES}	0.87 [-0.02, 1]	ms^{-1}
Activity coefficients[a]		
UVES		
$C_{\mathrm{H}\alpha}$	-0.24 [-1.02, 0.54]	
HARPS pre-2016		
$C_{\mathrm{H}\alpha}$	-0.63 [-4.13, 3.25]	
C_{He}	1.0 [-9.3, 11.4]	
C_{S}	-0.027 [-0.551, 0.558]	
C_{m_2}	-1.93 [-6.74, 2.87]	
C_{m_3}	0.82 [-0.60, 2.58]	
HARPS PRD		
$C_{\mathrm{H}\alpha}$	9.6 [-12.9, 33.3]	
C_{He}	-77 [-210, 69]	
C_{S}	-0.117 [-0.785, 0.620]	
C_{m_2}	-2.21 [-8.86, 7.96]	
C_{m_3}	-0.02 [-3.67, 3.44]	
PRD photometry		
C_{F}	0.0050 [-0.0183, 0.0284]	
$C_{\mathrm{F}'}$	-0.633 [-0.962, -0.304]	
$C_{\mathrm{FF}'}$	4.3 [-6.8, 14.8]	

[a]Units of the activity coefficients are ms^{-1}divided by the units of each activity index.